



Estimation and Tracking of AP-diameter of the Inferior Vena Cava in Ultrasound Images Using a Novel Active Circle Algorithm

Ebrahim Karami^{*a}, Mohamed Shehata^a, Andrew Smith^b

^aDepartment of Engineering and Applied Sciences, Memorial University, Canada,

^bFaculty of Medicine, Memorial University, Canada

Abstract

Medical research suggests that the anterior-posterior (AP)-diameter of the inferior vena cava (IVC) and its associated temporal variation as imaged by bedside ultrasound is useful in guiding fluid resuscitation of the critically-ill patient. Unfortunately, indistinct edges and gaps in vessel walls are frequently present which impede accurate estimation of the IVC AP-diameter for both human operators and segmentation algorithms.

The majority of research involving use of the IVC to guide fluid resuscitation involves manual measurement of the maximum and minimum AP-diameter as it varies over time. This effort proposes using a time-varying circle fitted inside the typically ellipsoid IVC as an efficient, consistent and novel approach to tracking and approximating the AP-diameter even in the context of poor image quality. In this active-circle algorithm, a novel evolution functional is proposed and shown to be a useful tool for ultrasound image processing. The proposed algorithm is compared with an expert manual measurement, and state-of-the-art relevant algorithms. It is shown that the algorithm outperforms other techniques and performs very close to manual measurement.

KEYWORDS: Inferior vena cava (IVC), ultrasound imaging, image segmentation, active circle, evolution functional, volume status, fluid responsiveness, resuscitation.

1. Introduction

Trauma patients suffering from hemorrhagic shock as a result of blood loss or patients with shortness of breath from volume overload in the setting of congestive heart failure frequently require immediate resuscitation. Fast and accurate assessment of circulating blood volume in critically-ill patients is a challenging task as excessive or insufficient fluid administration increases patient morbidity and mortality [1, 2]. Clinical research has shown that the variations in the anterior-posterior (AP) diameter of inferior vena cava (IVC) can be helpful in approximating a patient's volume status and whether or not they will benefit from additional intravenous fluids [3–5]. Traditionally, the AP-diameter is manually estimated from portable ultrasound imagery - often a challenging and time-consuming task in the setting of poor image quality. Artifacts such as shadowing and speckle noise frequently result in indistinct

^{*}Ebrahim karami is responsible for all correspondance (email:ekarami@mun.ca).

edges and gaps in the vessel walls reducing accurate estimation[6, 7].

Speckle noise present in ultrasound imagery is traditionally considered to be a Rayleigh distributed multiplicative noise [8]. Hence, Rayleigh mixture models have been proposed as a potential solution for ultrasound image segmentation [9, 10]. However, it has been shown that due to the scattering population and signal processing, the speckle distribution deviates from Rayleigh[11]. Furthermore, lossy compression algorithms present on many portable ultrasound machines further deviate the recorded clip from an idealized Rayleigh distribution.

Active contours (ACs), as planar deformable models, are widely used for segmentation of ultrasound images [12–16]. ACs address image segmentation through minimization of energy functional(s) with their performance frequently dependent on a manually-defined initialization contour. In order to avoid local minima, the initiating contour needs to be as close as possible to the actual contour. ACs can be combined with other segmentation algorithms as a coarse-to-fine strategy to reduce the impact of the initial contour on segmentation error [17, 18]. Researchers have addressed the challenge of IVC segmentation using this strategy by using template matching method as the coarse segmentation and AC as the fine-tuning (TMAC) [19]. Unfortunately, this approach fails when the IVC undergoes large frame-to-frame variations commonly present on portable machines with lower frame rates (e.g. 30 frames-per-second). Additionally, ACs continue to perform poorly in the context of fuzzy or unclear boundaries as is commonly the case for the IVC.

Given that the cross-section of the IVC is largely convex, the IVC contour can be represented in polar coordinates and consequently, polar active contours appear as a promising solution for IVC segmentation [20]. In [21], a polar AC model based on the third centralized moment (M3) was proposed for segmentation of IVC images. Unfortunately, M3 algorithms roughly estimates the cross-sectional area (CSA) of the IVC and fails with poor quality images.

Clinically the CSA of the IVC is an optimal approach to accurately assess a patient’s volume status, but all existing approaches fail to accurately estimate the CSA. Hence, clinicians instead of the the whole CSA of the IVC, measure its AP-diameter. In this paper, we propose using an active circle algorithm incorporating a novel evolution functional to estimate the AP-diameter of the IVC across a spectrum of image qualities. In addition, the proposed evolution functional appears promising for other ultrasound image segmentation problems as well.

The remainder of this paper is organized as follows - Section II discusses the background and related work. The proposed active circle algorithm is presented in Section III while experimental results are in Section IV and concluding remarks in Section V.

2. Background and Related work

2.1. IVC Image

Fig. 1 displays a typical ultrasound image of the IVC, with a circle fitted on the IVC AP-diameter shown in yellow color. For demonstrating the circle model which is later used in this work, we have also displayed two scaled circles, concentric with the yellow circle with scaling factors $S = 0.75$ and $S = 1.5$

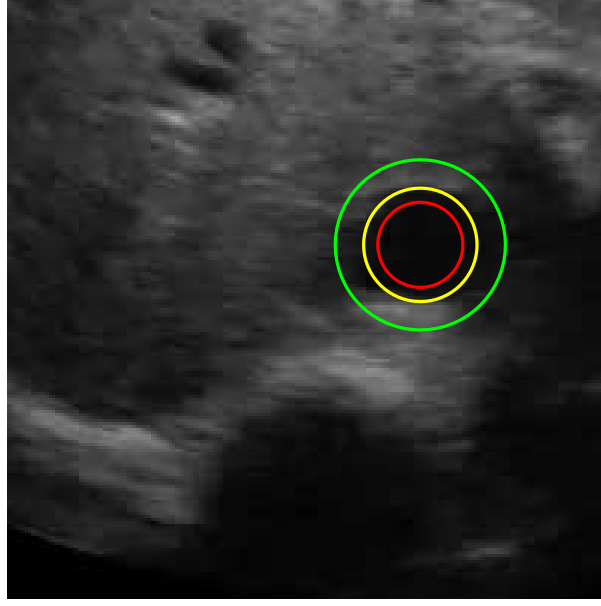


Figure 1: A typical ultrasound image of IVC with circle evolution model.

shown in red and green colors, respectively. As in Fig. 1, one can see that the IVC boundaries are generally fuzzy and are unclear. On the other hand, one can see that the inside of IVC is generally hypoechoic and the outside is hyperechoic indicating that the inside and outside of the IVC have distributions with different means. Fig. 2 illustrates the probability density functions (PDFs) of the intensity levels inside the three circles shown in Fig. 1, where the x-axis is the normalized pixel intensity which is between 0 and 1. From Fig. 2-(a) and (b), one can see that the intensity distribution inside the IVC contour is rather sparse than continuous. Assume that the intensity levels inside and outside the IVC have PDFs F_{in} with mean m_{in} and F_{out} with m_{out} , respectively. It is obvious that $m_{in} < m_{out}$. This indicates that regardless of the PDFs F_{in} and F_{out} , their distinct means can be used for image segmentation.

2.2. Energy and Evolution Functionals

In traditional level set methods for a given energy functional C , the evolution functional is obtained as [22, 23]:

$$\frac{\partial C}{\partial t} = -F(|\nabla C|), \quad (1)$$

where the function F depends on the image and is usually defined as a linear function. In this paper, we use the following linear function [22, 23]

$$E = -|\nabla C|\vec{n}, \quad (2)$$

where \vec{n} is the vector normal to the contour.

Two conventional functionals, widely employed in variational ACs, are based on the mean and the variance of the intensities [24].

Functional Based on Mean: Assuming u and v represent the mean intensity levels inside and outside the

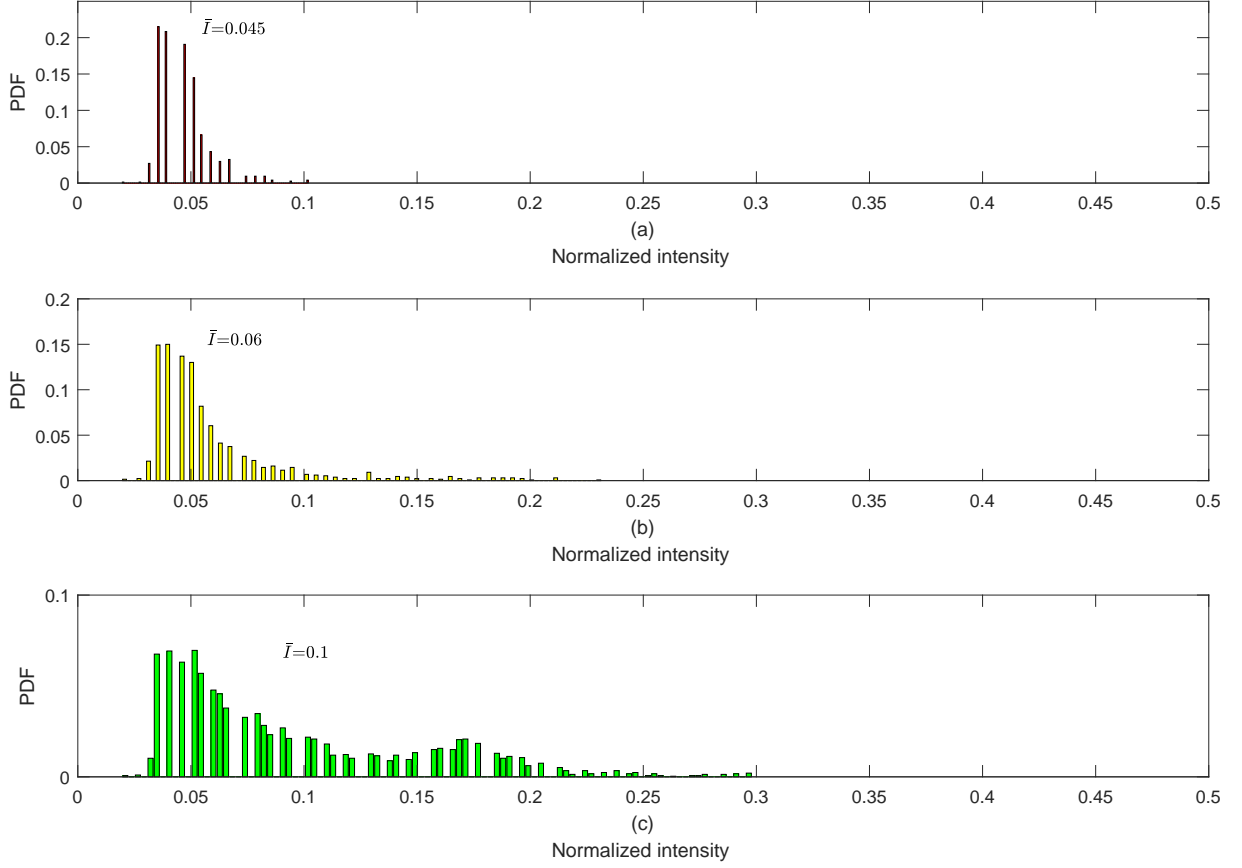


Figure 2: PDF of the intensity levels inside the disks concentric with the IVC (see Fig. 1) with radius equal to (a): 75%, (b): 100%, and (c): 150% of the IVC AP-diameter.

IVC, respectively, the energy functional is defined as [24]

$$C_{mean} = \frac{\alpha}{2}(u - v)^2, \quad (3)$$

where α is a positive weighting factor. Using (1), the evolution functional corresponding to (3) is obtained as [24]

$$E_{mean} = \alpha(u - v)\left(\frac{I - u}{A_u} + \frac{I - v}{A_v}\right)\vec{n}, \quad (4)$$

where I is the intensity at the contour point and A_u and A_v are the areas inside and outside the contour, respectively.

Functional Based on Variance: Assuming σ_u^2 and σ_v^2 as the variances of intensity levels inside and outside the IVC respectively, the energy functional is defined as [24]

$$C_{var} = \sigma_u^2 + \sigma_v^2, \quad (5)$$

Using (1), the evolution functional corresponding to (5) is obtained as

$$E_{var} = \alpha\left(\frac{I^2 - u^2 - \sigma_u^2}{A_u} - \frac{I^2 - v^2 - \sigma_v^2}{A_v}\right)\vec{n}, \quad (6)$$

where u and σ_u^2 are the mean and variance of the intensities for the pixels inside the contour while v and σ_v^2 represent for the ones outside the contour.

3. Proposed Algorithm

3.1. Why a Circular Model?

IVC images can be segmented with polar ACs as in [21]. When a polar AC with N contour points is used, the number of parameters that has to be estimated is N , i.e., one radial distance for each contour point, while with traditional Cartesian ACs, $2N$ parameters have to be estimated, i.e., two for x and y coordinates of each contour points. This makes polar contour models less complex and more accurate for vessel segmentation. On the other hand, to estimate the AP-diameter of the IVC, it is not necessary to fully segment the IVC contour; and hence, we can exploit a reduced model such as a circle which only has three parameters and, consequently, can be estimated more precisely. Fig. 3 shows four sample ultrasound images from IVCs with different shapes. For each case, the IVC contour is highlighted with yellow colors and its corresponding AP-diameter is shown with green colors. From Fig. 3, one can see that regardless of the shape of the IVC, a circle fitted inside it can accurately model and estimate the IVC AP-diameter.

3.2. Proposed Evolution Functional

After exploring a variety of energy and evolution functionals, we heuristically found the following evolution functional to be useful for segmentation of ultrasound images.

$$E = \alpha(u - v)(2I - u - v). \quad (7)$$

With the model defined in Section II.A, it is easy to see that if the contour is entirely inside the IVC, then $\bar{I} = u = m_{in}$, with \bar{I} being the average intensity for the points on the contour. Consequently, the evolution functional for contour points is a random variable with the mean value

$$\bar{E} = (u - v)(2\bar{I} - u - v) = (u - v)^2, \quad (8)$$

resulting in the contour consistently expanding toward the actual IVC boundary. On the contrary, if the contour is entirely outside the IVC, then $\bar{I} = v = m_{out}$ and the evolution functional for contour points is a random variable with the mean value

$$\bar{E} = (u - v)(2\bar{I} - u - v) = -(u - v)^2, \quad (9)$$

resulting in the contour consistently shrinking toward the actual IVC boundary.

To support this finding, we computed the sensitivity of the proposed evolution functional to translation and scaling of the fitted circle.

Fig. 4 shows this results with the y-axis being the average contour evolution for the points on fitted circle with $\alpha = 10^{-3}$. Fig. 4-(a) shows this averaged functional when the circle diameter equals to AP-diameter but its center is shifted by δ_x along the x-axis. From 4-(a), one can see that when the fitted circle is shifted toward the left, i.e, with $\delta_x < 0$, the average evolutionary functional is positive, moving the fitted circle to the right, and vice versa. The circle evolution only stops when the average evolutionary functional is zero which occurs at $\delta_x = 0$. One can see a similar result for the transverse axis in Fig. 4-(b). This proves that with the proposed \bar{E} evolutionary functional, the algorithm reaches equilibrium when the

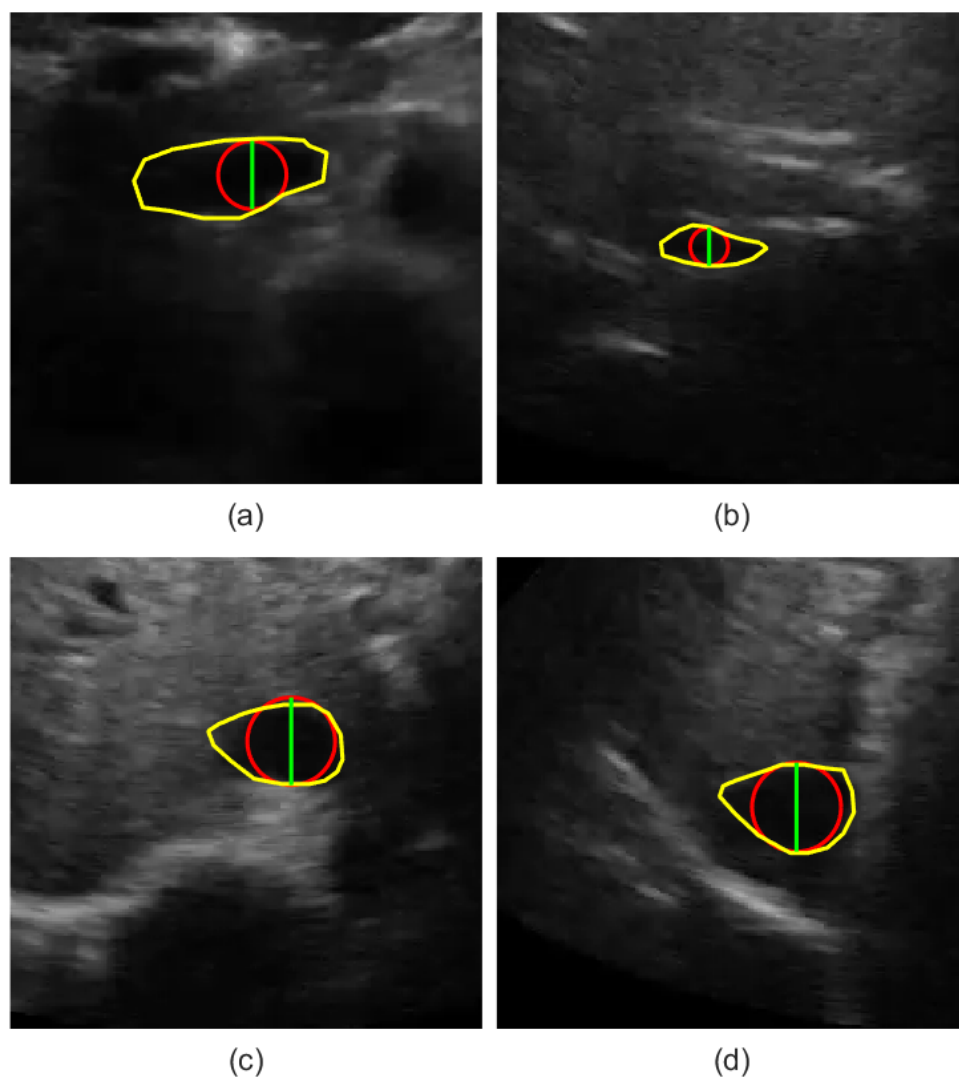


Figure 3: Estimation of AP-diameter using circle fitting in IVC images with different shapes and qualities.

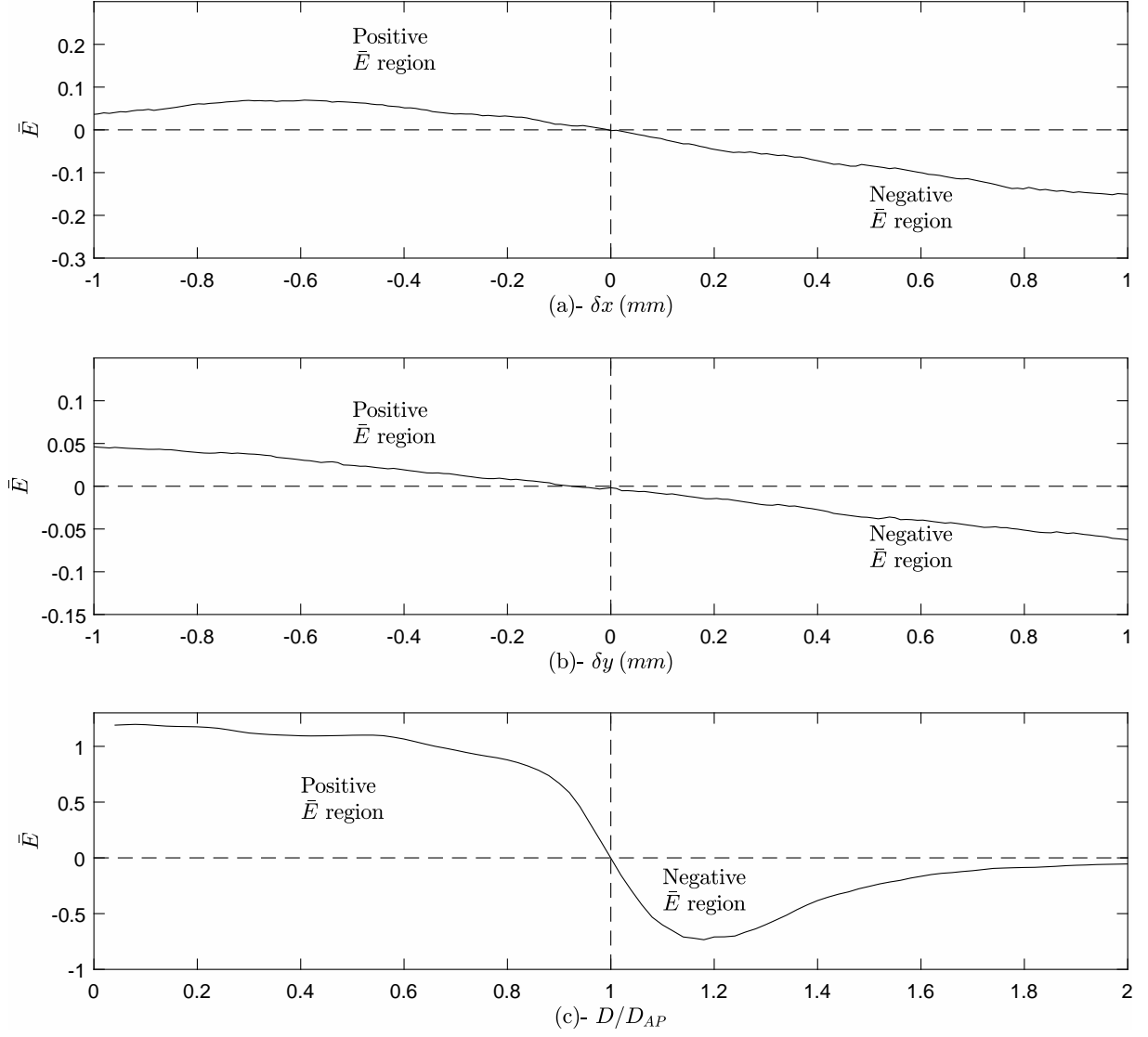


Figure 4: Proposed evolution functional versus (a)- δx , (b)- δy , and (c)- normalized circle diameter D/D_{AP} with $\alpha = 10^{-3}$.

circle centers on the IVC. Fig. 4-(c) shows this result versus the circle diameter, i.e., functional averaged over the points on the circle with diameter D and concentric with the IVC center. From Fig. 4-(c), one can see that when the circle diameter is less than D_{AP} of the IVC, the evolutionary functional is positive demonstrating that the contour is expanding toward the actual IVC boundaries. This proves that with the proposed functional, the algorithm reaches its equilibrium if $D = D_{AP}$, i.e., when the diameter of the circle equals to the actual AP-diameter of the vessel.

3.3. Circle Evolution

The evolution functional is utilized to update the parameters of the circle with R and (x_c, y_c) as its radius and center, respectively. Initially, the circle is sampled at K points with polar angles $\theta_k = \frac{2k\pi}{N}$, $k = 0, 1, \dots, K-1$, where the normal vector and Cartesian coordinates corresponding to the k th sampled



Figure 5: The forces generated by the evolution functional in (7) with $\alpha = 0.05$ and $K = 8$ (values are adjusted for illustration purposes).

point notated as

$$\vec{n}_k = [\cos(\theta_k), \sin(\theta_k)]^T, \quad (10)$$

and

$$[x_k, y_k]^T = [x_c, y_c]^T + R\vec{n}_k, \quad (11)$$

respectively. The evolution functional generates forces $f_k = \alpha(u-v)(2I_k - u - v)$ along the normal vectors $n_k, k = 0, 1, \dots, K-1$, as shown in Fig. 5. The forces shift the sampled contour points to new positions governed by

$$[\tilde{x}_k, \tilde{y}_k] = [x_c, y_c]^T + (R + f_k)\vec{n}_k. \quad (12)$$

where f_k is the value of the evolution functional at k th contour point. Obviously, the shifted contour points are not on a circle anymore; hence, a new circle needs to be fitted to the updated contour points. This is accomplished through minimization of the following energy functional:

$$C_{circle} = \sum_{k=0}^{K-1} [(\tilde{x}_k - \tilde{x}_c - \tilde{R}\cos(\theta_k))^2 + (\tilde{y}_k - \tilde{y}_c - \tilde{R}\sin(\theta_k))^2], \quad (13)$$

where $[\tilde{x}_c, \tilde{y}_c]$ and \tilde{R}_c are the center and radius of the updated circle. By minimizing C_{circle} , the new values for the center and radius of the circle are obtained using the following theorems.

Theorem 1. For a given set of forces, the circle center is shifted by the average of the force vectors $f_k\vec{n}_k$.

PROOF. To find \tilde{x}_c and \tilde{y}_c , the energy functional (C_{circle}) in (13) is minimized by setting its gradient to

zero as:

$$\frac{\partial C_{circle}}{\partial \tilde{x}_c} = -2 \sum_{k=0}^{K-1} (\tilde{x}_k - \tilde{x}_c - \tilde{R} \cos(\theta_k)) = 0, \quad (14)$$

$$\frac{\partial C_{circle}}{\partial \tilde{y}_c} = -2 \sum_{k=0}^{K-1} (\tilde{y}_k - \tilde{y}_c - \tilde{R} \sin(\theta_k)) = 0. \quad (15)$$

Since $\sum_{k=0}^{K-1} \cos(\theta_k) = \sum_{k=0}^{K-1} \sin(\theta_k) = 0$, by substituting (13) in (14) and (15), one can easily find

$$[\tilde{x}_c, \tilde{y}_c] = [x_c, y_c] + \frac{1}{K} \sum_{k=0}^{K-1} f_k \vec{n}_k, \quad (16)$$

highlighting that the circle center is shifted by the average of the force vectors $f_k \vec{n}_k$.

Theorem 2. For a given set of forces, the circle radius is modified with the average of the force values f_k .

PROOF. To find the new circle radius \tilde{R} , the energy functional (C_{circle}) in (13) is minimized by setting its gradient to zero as:

$$\begin{aligned} \frac{\partial C_{circle}}{\partial \tilde{R}} &= -2 \sum_{k=0}^{K-1} [(\tilde{x}_k - \tilde{x}_c - \tilde{R} \cos(\theta_k)) \cos(\theta_k) \\ &+ (\tilde{y}_k - \tilde{y}_c - \tilde{R} \sin(\theta_k)) \sin(\theta_k)] = 0. \end{aligned} \quad (17)$$

By substituting (16) in (17), one determines that

$$\tilde{R} = R + \frac{1}{K} \sum_{k=0}^{K-1} f_k. \quad (18)$$

3.4. Proposed Active Circle Algorithm

In this paper we set $K = 32$ and $\alpha = 10^{-4}$. Note that with a larger value of K , the estimation accuracy is improved at the cost of increased computational complexity. Similarly, with a smaller value of α the accuracy is improved at the cost of increased number of iterations required to reach the convergence. The flowchart of the algorithm is shown in Fig. 6. As the first step, the proposed algorithm requests to manually locate the IVC. This is simply performed by a mouse click on a point inside the IVC. The initial circle centers at this selected point and to avoid convergence to a wrong boundary, its radius is assumed to be as small as 6 pixels. In the second step, we compute the forces f_k using (7). In the third step, these forces to evolve the circle parameters using (16) and (18). Steps two and three are repeated until either a convergence or maximum number of iterations, i.e., 5000 iterations is achieved. In this paper, we assume the algorithm has converged, if the largest force computed in the second step is less than 10^{-3} pixels. This process is repeated for the next frames of the videos.

3.5. Complexity Analysis

The complexity of the proposed active circle algorithm is obviously much less than the state-of-the-art algorithms. The algorithm obtains its low complexity from: 1) the simplicity of the proposed evolutionary 2) the simplicity of the circle model which only has three parameters to estimate. In this

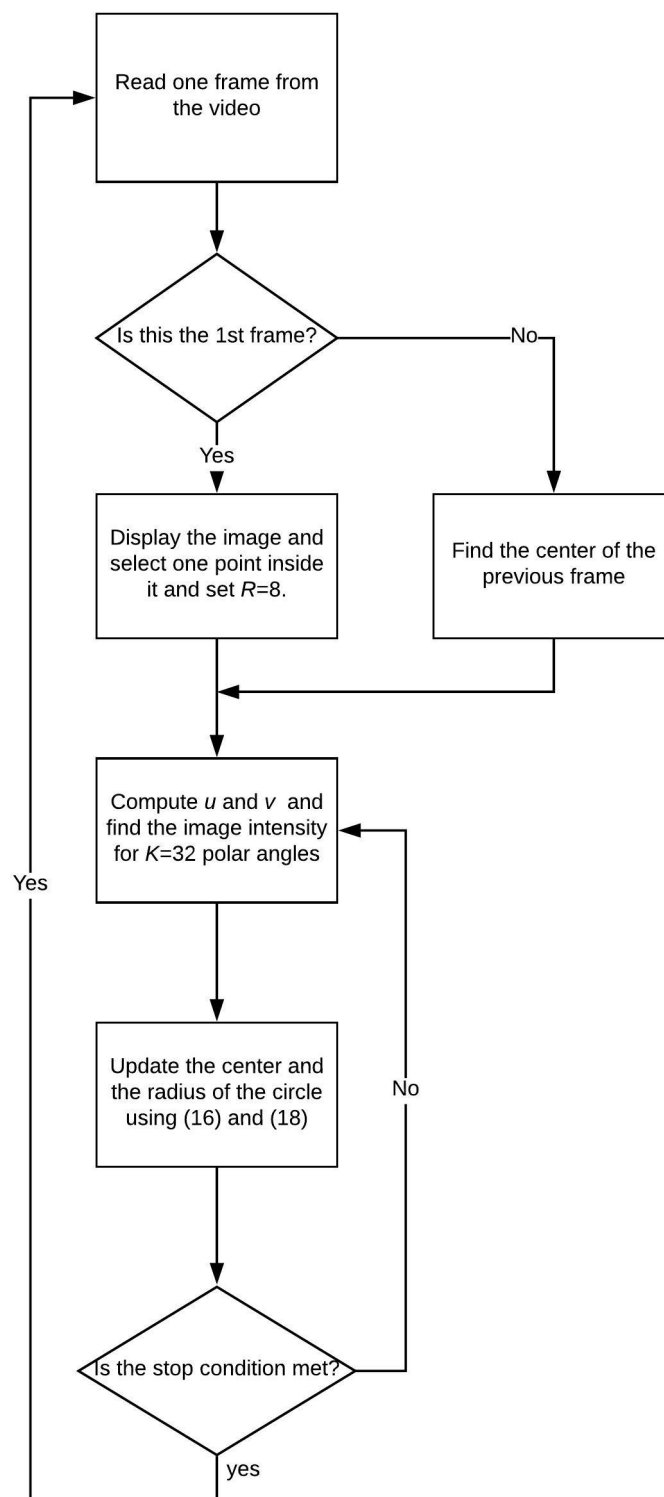


Figure 6: Flowchart of the proposed active-circle algorithm.



Figure 7: First frame of three sample IVC videos rated as (a)- good, (b)- average, and (c)- poor quality videos.

Section, we estimate the computational complexity of the active-circle algorithm using the number of floating point operations (flops) [25]. Assume N_{iter} as the average number of iterations and $A_{max} = 5000$ pixels as the maximum area of the circle. From equations (7), (16), and (18), one can see that the maximum number of flops for each frame is $N_{flops} = (2A_{max} + 3K + 5)N_{iter} \approx 50$ million flops, i.e., with an average i7-3770 Intel processor, estimation of AP-diameter from each frame requires less than 1 millisecond.

4. Results

The experimental data was collected from eight healthy male subjects with ages from 21 to 35. The study protocol was reviewed and approved by the Health Research Ethics Authority. The IVC was imaged in the transverse plane using a portable ultrasound (M-Turbo, Sonosite-FujiFilm) with a phased-array probe (1-5 Mhz). Each video has a frame rate of 30 fps, scan depth of 19cm, and a duration of 15 seconds (450 frames/clip). Fig. 7 depicts the first frame of three subjects with different qualities which are graded, based on their quality and clinical impression, by three experts, including Dr. Andrew Smith as a point-of-care ultrasound expert and two additional clinicians. Note that although the sample image in Fig. 7-(b) seems to have a better quality than the one in Fig. 7-(a), it is rated as average quality due to its more fuzzy boundaries which degraded the accuracy of the algorithm.

4.1. Comparison of the proposed functional with state-of-the-art functionals

In this Section, we first compare the proposed evolution functional with manual measurements made by Dr. Andrew Smith, and two state-of-the-art evolution functionals in eqs. (4) and (6). From Fig. 8, one can see that in all three investigated videos, the active circle algorithm using the two state-of-the-art functionals fail to track the relatively fast AP-diameter variations in the first video. This is because, in IVC images $A_u \ll A_v$, and hence in eqs. (4) and (6), the second term is dominated by the first term. Consequently, the balance between the intensities inside and outside the contour is not established. Note that in Fig. 8-(c) which presents the results for the third subject, due to the extremely poor quality of this video, the manual measurement is partially missing for the frames in range 297 to 332, as the expert was unable to measure the AP-diameter. The proposed algorithm still estimate the AP-diameter although there is no ground truth for these frames.

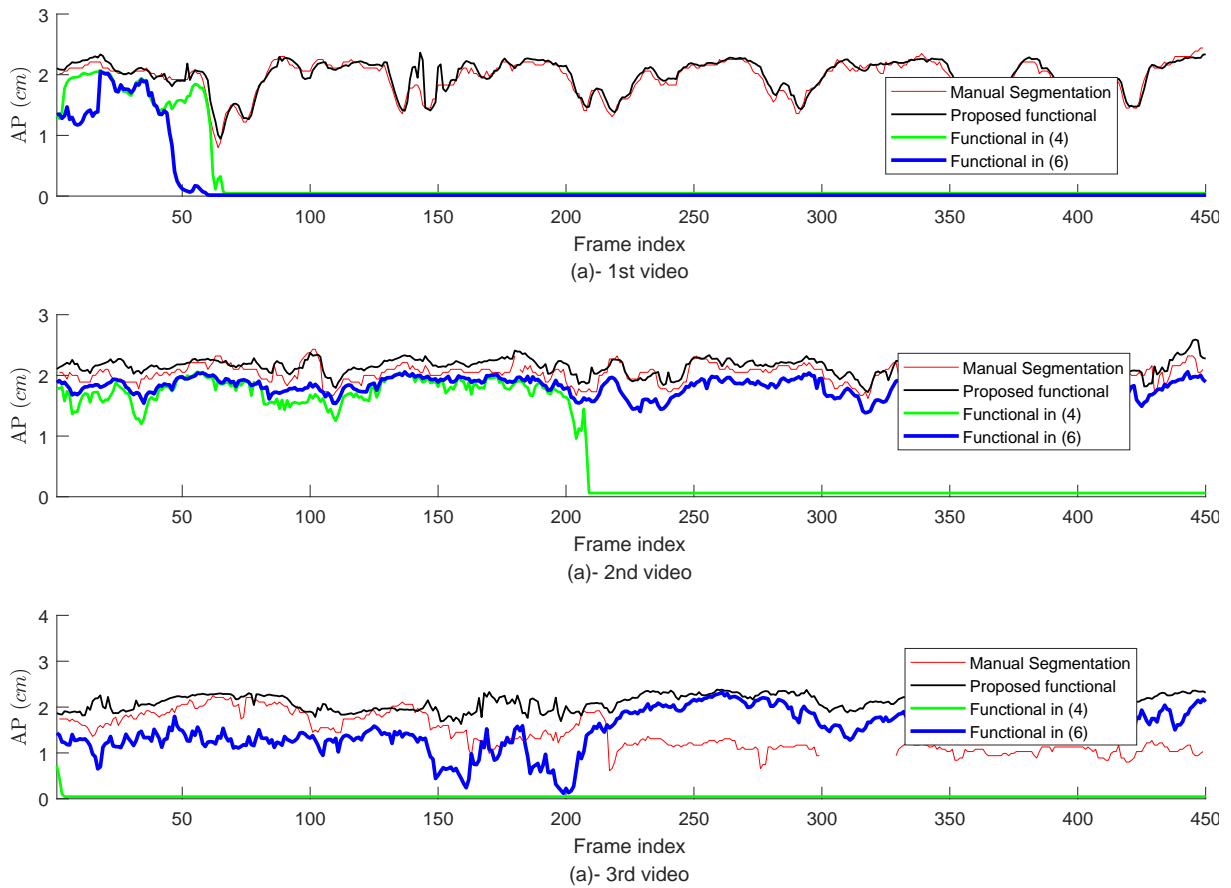


Figure 8: IVC diameter of a typical IVC video as measured by the proposed functional and two functionals in equations (4) and (6).

4.2. Influence of the parameter α on the accuracy of the proposed algorithm

In this section, we investigate the sensitivity of the proposed algorithm to the value of α for the three videos depicted in Fig. 7. For this study, we use root mean square (RMS) of error as the performance criterion, with the error e defined as the difference between the AP-diameter estimated from the proposed algorithm and the manual measurement. For the first two subjects, the RMS of error is calculated over all 450 frames, but for the third video, it is calculated over the first 150 frames, where the manual measurement seems to be reliable. From Fig. 9, one can easily see that in all three cases, the proposed algorithm performs well with $\alpha < 5 \times 10^{-4}$. Hence, for the rest of our experiments, we set $\alpha = 10^{-4}$. Note that with a smaller α , more accurate results can be obtained in the cost of more number of iterations required for convergence.

4.3. comparison of the proposed algorithm with state-of-the-art segmentation algorithms

The proposed active circle algorithm was also compared with expert manual measurement, the two classic AC algorithms - Chan-Vese [26] and Geodesic [27], and four state-of-the-art polar ACs- PSnake [28] and variational polar AC [29], M3 algorithm [21], and Ad-PAC [31], and star-Kalman algorithm [32].

Fig. 10-(a) presents the results for the video depicted in Fig. 7-(a). This figure illustrates that only the

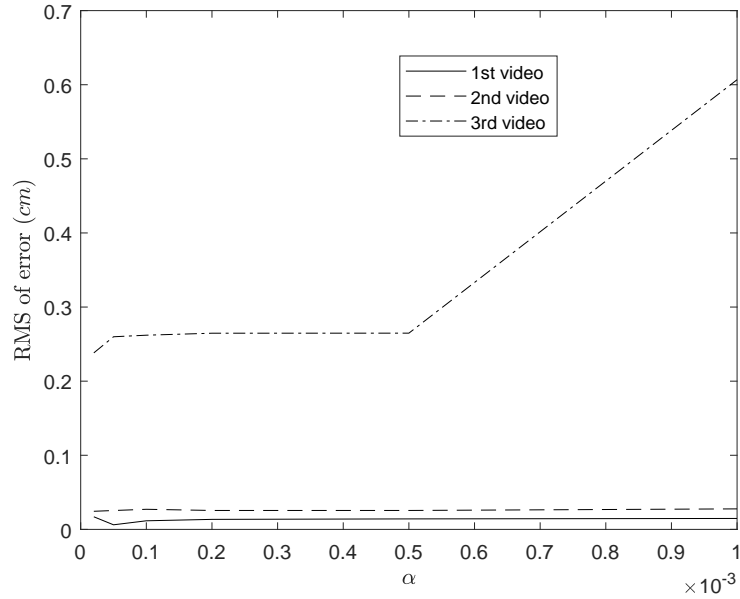


Figure 9: The RMS of error for the proposed algorithm w.r.t. the parameter α for the three sample videos depicted in Fig. 7.

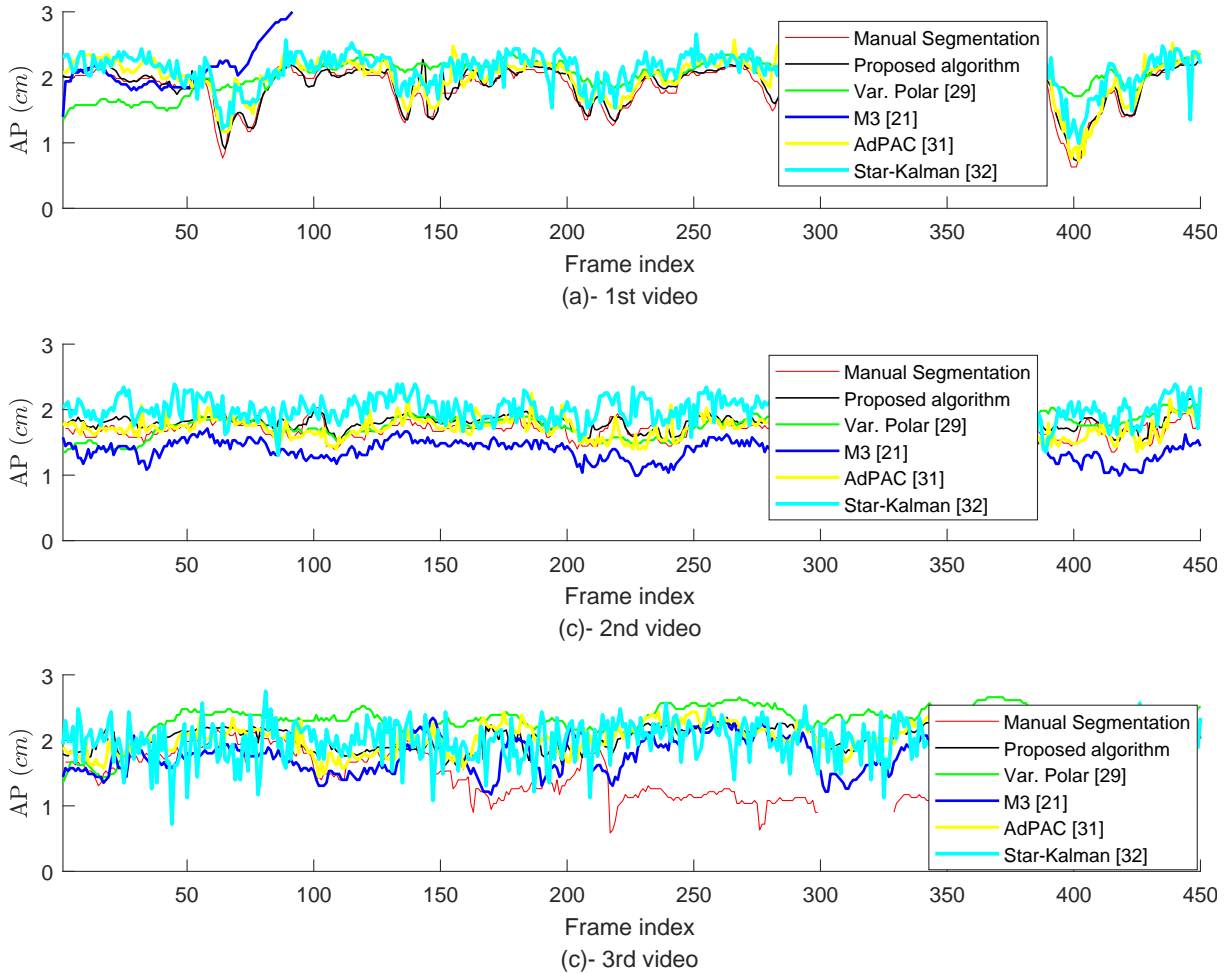


Figure 10: AP-diameter for the three samples videos depicted in Fig. 7, as measured by the proposed algorithm, manual extraction, and four other algorithms.

active circle accurately tracks and segments the IVC and follows the variations in manual extraction. M3 algorithm fails to track, whereas the others struggle to capture the temporal variation.

Fig. 10-(b) details the results for the video depicted in Fig. 7-(b) which suffers from artifact partially occluding the vessel wall. Here, it is evident that the proposed algorithm again tracks the temporal variations of the manual extraction.

Fig. 10-(c) details the results for the video depicted in Fig. 7-(c) which has a poor quality (the worst among all eight investigated videos). In this case, both the proposed algorithm and manual extraction roughly estimated the AP-diameter for the first 150 frames and then they failed.

Table 1 presents the RMS of the AP-diameter estimation error for the proposed algorithm and other seven algorithms and for all eight studied subjects, with the last column showing the results averaged over all subjects. Note that videos no. 1 to 3 are the ones depicted in Fig. 7. Except the third subject where the manual measurement is reliable only for the first 150 frames (see Fig. 10-(c)), for the other seven subject, the RMS of error is calculated over all 450 frames. From this table, one can see that for all eight studies subjects, the proposed algorithm outperforms other seven methods. The second best performance is obtained from M3 algorithm. One can also see that the Star-Kalman algorithm which fits an ellipse to the IVC contour performs much poorer than the proposed active-circle algorithm. The worst average performance is obtained from the two classic AC algorithms, i.e., Chan-Vese and Geodesic AC, showing that polar ACs perform in average more accurate than the Cartesian ACs because their larger degree of freedom, i.e, the number of parameters that has to be estimated.

Table 1: RMS of the AP-diameter estimation error obtained using the proposed algorithm and seven other methods.

Subject no. \ Method	1	2	3	4	5	6	7	8	Ave
Proposed algorithm	0.10	0.16	0.26	0.16	0.25	0.25	0.1	0.11	0.17
Var. Polar [29]	0.38	0.25	0.49	0.27	0.42	0.28	0.24	0.52	0.36
Psnake [28]	0.66	0.50	0.52	0.5	0.4	0.33	0.49	0.71	0.51
M3 [21]	0.53	0.30	0.24	0.30	0.31	0.32	0.41	0.42	0.35
AdPAC [31]	0.21	0.17	0.2	0.17	0.16	1.1	1.8	0.13	0.39
Star-Kalman [32]	0.34	0.45	0.44	0.45	0.58	0.54	0.37	0.25	0.43
Chan-Vese [26]	1.77	0.39	0.54	0.39	0.38	0.33	0.55	0.73	0.66
Geodesic [27]	1.89	0.17	0.54	0.17	0.38	0.33	0.55	0.73	0.60

4.4. More Comparison Metrics

In table 2, we compare the proposed algorithm and manual estimation using more metrics, where some of these metrics are also clinically useful to assess patient's status. In this table, e_{ave} is the average estimation error, averaged over the frames in each video; σ_e is the standard deviation of the estimation error e for the frames in each video, and $|e|_{max}$ is the maximum error. Note that e_{ave} , except for the third subject where only the manual measurements for the first 150 frames are reliable, is calculated over all 450 frames. Since the values of D_{max} and D_{min} are useful for the medical purposes, we have also

compared them obtained from both the algorithm and manual measurement. Note that subjects no. 1 to 3 are the ones depicted in Fig. 7. Furthermore, note that for subject no. 3, i.e., the lowest quality video, these metrics are only calculated for the first 150 frames, where the manual extraction is relatively reliable, while for other seven subjects, they are computed over all 450 frames. From table 2, one can see that except for the fourth subject, in other cases, D_{max} estimated from the proposed algorithm is very close to the one obtained from the manual measurement and for 5 out of the eight studied subjects, the error for estimation of D_{max} is less than 2mm. Furthermore, in all cases the average error is positive indicating that the proposed algorithm usually overestimates the AP-diameter although this bias is very small and is mostly less than 2mm. Note that this overestimation is mainly due to the fact that the expert extracts the AP-diameter from the inside boundary of IVC. The amount of bias can simply be controlled by adding a constant value to the functional. In all cases, the value σ_e is small indicating that the proposed algorithm performs consistent over different frames of each video.

Table 2: Summary of the results of eight studied IVC videos.

Subject no.	1	2	3	4	5	6	7	8
e_{ave} (cm)	0.03	0.07	0.07	0.18	0.29	0.37	0.04	0.08
σ_e (cm)	0.06	0.07	0.14	0.08	0.08	0.13	0.09	0.11
$ e _{max}$ (cm)	0.06	0.29	0.43	0.48	0.57	0.75	0.41	0.44
D_{max} alg. (cm)	2.39	2.59	2.3	1.93	2.35	2.29	2.14	2.33
D_{min} alg. (cm)	0.67	0.75	1.7	1.37	1.69	1.38	1.54	1.16
D_{max} man. (cm)	2.43	2.43	2.25	2.41	2.36	2.08	2.21	2.39
D_{min} man. (cm)	0.7	0.66	1.36	0.94	1.34	1.22	1.42	1.21

4.5. Influence of speckle removal filtering on the performance of the proposed algorithm

In this subsection, we investigate the influence of different speckle-removal filters on the performance of the proposed algorithm. For this study, we used the proposed algorithm for the images smoothed by either of the the following filters: Bilateral filter [33], 3D block matching filter (BM3D) [34], speckle reducing anisotropic diffusion (SRAD) [35], Wiener filter [36], and median filter.

Fig. 11 shows the AP-diameter estimated using the proposed algorithm with each of the above speckle removal filters and have shown their results for the subjects depicted in Fig. 7. From Fig. 11, one can see that none of these filtering techniques significantly improve the performance of the proposed algorithm. This is mainly due to the fact that the speckle noise in ultrasound images includes useful information that can even improve the performance of computerized algorithms. On the other hand, as it was discussed in Section III, the proposed algorithm relies on the mean value of the local distributions which usually is not significantly changed by speckle removal filters.

Table 3 presents numerical results to validate this argument. One can see that except bilateral filter,

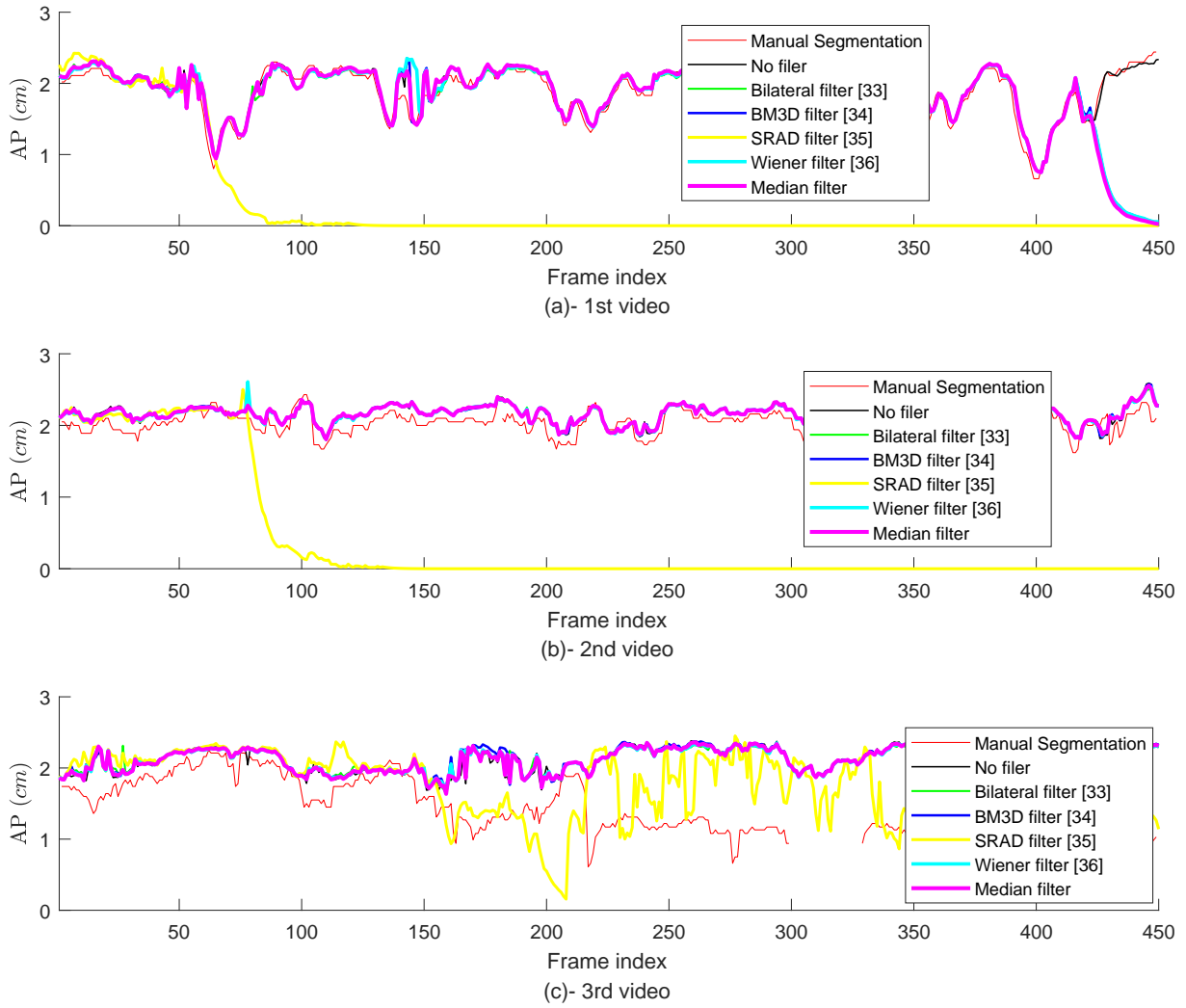


Figure 11: Estimated AP-diameter versus the type of speckle removal filter.

other speckle-removal filters even degrade the performance and the improvement obtained from bilateral filter is negligible.

Table 3: RMS of error obtain from the proposed algorithm with different speckle removal filters.

Metric \ Subject no.	Subject no.							
	1	2	3	4	5	6	7	8
No. filter	0.10	0.16	0.26	0.33	0.25	0.25	0.10	0.12
Bilateral filter [33]	0.11	0.16	0.28	0.32	0.24	0.24	0.10	0.11
BM3D [34]	0.48	0.16	0.27	0.41	0.68	0.26	0.10	0.11
SRAD [35]	1.78	1.81	0.34	0.50	0.78	0.73	0.10	0.11
Wiener filter [36]	0.48	0.17	0.26	0.34	0.43	0.25	0.10	0.12
Median filter	0.48	0.17	0.26	0.36	0.53	0.25	0.10	0.12

5. Conclusion

In this paper, a novel active circle algorithm is developed for estimating the AP-diameter of the IVC in ultrasound imagery. It has been shown that the diameter of a circle fitted inside the IVC can accurately model the AP-diameter and therefore, is a useful tool capable of supporting further clinical research of using the IVC to guide fluid resuscitation. Furthermore, a novel evolution functional has been proposed and used for updating the circle parameters. Experimental results suggest that the proposed algorithm performs very close to the expert manual measurements. The proposed algorithm only failed under extremely low image-quality scenarios when the AP-diameter was even unable to be measured by the expert.

References

- [1] V. Smyrniotis, G. Kostopanagiotou, K. Theodoraki, D. Tsantoulas, J. C. Contis, The role of central venous pressure and type of vascular control in blood loss during major liver resections, *The American journal of surgery* 187 (3) (2004) 398–402.
- [2] E. Rivers, B. Nguyen, S. Havstad, J. Ressler, A. Muzzin, B. Knoblich, E. Peterson, M. Tomlanovich, Early goal-directed therapy in the treatment of severe sepsis and septic shock, *New England Journal of Medicine* 345 (19) (2001) 1368–1377.
- [3] C. Charron, V. Caille, F. Jardin, A. Vieillard-Baron, Echocardiographic measurement of fluid responsiveness, *Current opinion in critical care* 12 (3) (2006) 249–254.
- [4] L. Durairaj, G. A. Schmidt, Fluid therapy in resuscitated sepsis: less is more, *Chest Journal* 133 (1) (2008) 252–263.
- [5] C. Barbier, Y. Loubières, C. Schmit, J. Hayon, J.-L. Ricôme, F. Jardin, A. Vieillard-Baron, Respiratory changes in inferior vena cava diameter are helpful in predicting fluid responsiveness in ventilated septic patients, *Intensive care medicine* 30 (9) (2004) 1740–1746.
- [6] W. Wang, L. Zhu, J. Qin, Y.-P. Chui, B. N. Li, P.-A. Heng, Multiscale geodesic active contours for ultrasound image segmentation using speckle reducing anisotropic diffusion, *Optics and Lasers in Engineering* 54 (2014) 105–116.
- [7] S. Sudha, G. Suresh, R. Sukanesh, Speckle noise reduction in ultrasound images by wavelet thresholding based on weighted variance, *International journal of computer theory and engineering* 1 (1) (2009) 7.
- [8] R. F. Wagner, S. W. Smith, J. M. Sandrik, H. Lopez, Statistics of speckle in ultrasound b-scans, *IEEE transactions on sonics and ultrasonics* 30 (3) (1983) 156–163.
- [9] J. C. Seabra, F. Ciompi, O. Pujol, J. Mauri, P. Radeva, J. Sanches, Rayleigh mixture model for plaque characterization in intravascular ultrasound, *IEEE Transactions on Biomedical Engineering* 58 (5) (2011) 1314–1324.
- [10] M. Pereyra, N. Dobigeon, H. Batatia, J.-Y. Tourneret, Segmentation of skin lesions in 2-d and 3-d ultrasound images using a spatially coherent generalized rayleigh mixture model, *IEEE transactions on medical imaging* 31 (8) (2012) 1509–1520.
- [11] T. Tuthill, R. Sperry, K. Parker, Deviations from rayleigh statistics in ultrasonic speckle, *Ultrasonic imaging* 10 (2) (1988) 81–89.
- [12] M. Kass, A. Witkin, D. Terzopoulos, Snakes: Active contour models, *International journal of computer vision* 1 (4) (1988) 321–331.
- [13] E. Karami, M. Shehata, P. McGuire, A. Smith, A semi-automated technique for internal jugular vein segmentation in ultrasound images using active contours, in: *2016 IEEE-EMBS International Conference on Biomedical and Health Informatics (BHI)*, IEEE, 2016, pp. 184–187.
- [14] B. Liu, H. Cheng, J. Huang, J. Tian, X. Tang, J. Liu, Probability density difference-based active contour for ultrasound image segmentation, *Pattern Recognition* 43 (6) (2010) 2028–2042.
- [15] M. Talebi, A. Ayatollahi, A. Kermani, Medical ultrasound image segmentation using genetic active contour, *Journal of Biomedical Science and Engineering* 4 (02) (2011) 105.
- [16] J. A. Noble, Ultrasound image segmentation and tissue characterization, *Proceedings of the Institution of Mechanical Engineers, Part H: Journal of Engineering in Medicine* 224 (2) (2010) 307–316.
- [17] P. J. Yim, D. J. Foran, Volumetry of hepatic metastases in computed tomography using the watershed and active contour algorithms, in: *Computer-Based Medical Systems, 2003. Proceedings. 16th IEEE Symposium*, IEEE, 2003, pp. 329–335.

- [18] S. Ali, A. Madabhushi, An integrated region-, boundary-, shape-based active contour for multiple object overlap resolution in histological imagery, *IEEE transactions on medical imaging* 31 (7) (2012) 1448–1460.
- [19] K. Nakamura, M. Tomida, T. Ando, K. Sen, R. Inokuchi, E. Kobayashi, S. Nakajima, I. Sakuma, N. Yahagi, Cardiac variation of inferior vena cava: new concept in the evaluation of intravascular blood volume, *Journal of Medical Ultrasonics* 40 (3) (2013) 205–209.
- [20] M. Baust, et al., Polar active contours for medical applications, Ph.D. thesis, Technische Universität München (2012).
- [21] E. Karami, M. Shehata, A. Smith, Segmentation and tracking of inferior vena cava in ultrasound images using a novel polar active contour algorithm, in: 5th IEEE Global Conference on Signal and Information Processing, GlobalSIP2017, IEEE, 2017, pp. 1–5.
- [22] C. Li, C. Xu, C. Gui, M. D. Fox, Level set evolution without re-initialization: a new variational formulation, in: *Computer Vision and Pattern Recognition, 2005. CVPR 2005. IEEE Computer Society Conference on*, Vol. 1, IEEE, 2005, pp. 430–436.
- [23] D. Cremers, S. J. Osher, S. Soatto, Kernel density estimation and intrinsic alignment for shape priors in level set segmentation, *International journal of computer vision* 69 (3) (2006) 335–351.
- [24] A. Yezzi, L. Zöllei, T. Kapur, A variational framework for integrating segmentation and registration through active contours, *Medical image analysis* 7 (2) (2003) 171–185.
- [25] D. S. Watkins, *Fundamentals of matrix computations*, Vol. 64, John Wiley & Sons, 2004.
- [26] T. F. Chan, L. A. Vese, Active contours without edges, *IEEE Transactions on image processing* 10 (2) (2001) 266–277.
- [27] V. Caselles, R. Kimmel, G. Sapiro, Geodesic active contours, *International journal of computer vision* 22 (1) (1997) 61–79.
- [28] A. R. De Alexandria, P. C. Cortez, J. A. Bessa, J. H. da Silva Felix, J. S. De Abreu, V. H. C. De Albuquerque, psnakes: A new radial active contour model and its application in the segmentation of the left ventricle from echocardiographic images, *Computer methods and programs in biomedicine* 116 (3) (2014) 260–273.
- [29] M. Baust, A. J. Yezzi, G. Unal, N. Navab, A sobolev-type metric for polar active contours, in: *Computer Vision and Pattern Recognition (CVPR), 2011 IEEE Conference on*, IEEE, 2011, pp. 1017–1024.
- [30] E. Karami, M. Shehata, A. Smith, Tracking of the Internal Jugular Vein in Ultrasound Images Using Optical Flow, in: *The 30th Annual IEEE Canadian Conference on Electrical and Computer Engineering (CCECE)*, IEEE, 2016, pp. 184–187.
- [31] E. Karami, M. S. Shehata, A. Smith, Adaptive polar active contour for segmentation and tracking in ultrasound videos, *IEEE Transactions on Circuits and Systems for Video Technology*, doi : 10. 1109/TCSVT. 2018. 2818072.
- [32] J. Guerrero, S. E. Salcudean, J. A. McEwen, B. A. Masri, S. Nicolaou, Real-time vessel segmentation and tracking for ultrasound imaging applications, *IEEE transactions on medical imaging* 26 (8) (2007) 1079–1090.
- [33] C. Tomasi, R. Manduchi, Bilateral filtering for gray and color images, in: *Computer Vision, 1998. Sixth International Conference on*, IEEE, 1998, pp. 839–846.
- [34] K. Dabov, A. Foi, V. Katkovnik, K. Egiazarian, Image denoising by sparse 3-d transform-domain collaborative filtering, *IEEE Transactions on image processing* 16 (8) (2007) 2080–2095.
- [35] Y. Yu, S. T. Acton, Speckle reducing anisotropic diffusion, *IEEE Transactions on image processing* 11 (11) (2002) 1260–1270.
- [36] C. P. Loizou, C. S. Pattichis, Despeckle filtering algorithms and software for ultrasound imaging, *Synthesis lectures on algorithms and software in engineering* 1 (1) (2008) 1–166.